



Strain Analysis of Multi-Phase Steel Using In-Situ EBSD Tensile Testing and Digital Image Correlation

Kyung Il Kim^{1,2} · Yeonju Oh¹ · Dong Uk Kim¹ · Joo-Hee Kang³ · Nam Ik Cho⁴ · Kyu Hwan Oh¹ · Jun-Yun Kang³ · Heung Nam Han¹

Received: 11 May 2021 / Accepted: 12 May 2021 / Published online: 3 September 2021
© The Korean Institute of Metals and Materials 2021

Abstract

An in-situ analysis of local strain accommodation on transformation induced plasticity (TRIP) aided multi-phase steel was performed with a correlative application of characterization techniques such as digital image correlation (DIC), electron backscatter diffraction (EBSD), and micro-mechanical testing. The local strain on the complex microstructure of the multi-phase steel was measured during a tensile test using an innovative DIC method (which does not employ artificial patterns), in conjunction with a scanning electron microscope. The constituent phases of the examined surface were identified by postprocessing implemented on the EBSD maps. This was further verified by nano-indentation, consequently enabling systematic and quantitative analyses of the strain partitioning between the phases. Soft acicular ferrite accommodated the largest strain with sites of intense strain localization around the hard, neighboring martensite. The retained austenite transformed gradually into martensite because of the applied strain and caused strain localization in the neighboring acicular ferrite. This verified that DIC method proposed in this study enables precise and effective data collection at the interfaces between different phases that could have certainly been blocked by the DIC patterns in the conventional method.

Keywords Digital image correlation · Microstructure · Electron backscatter diffraction · In-situ test

1 Introduction

The use of high-strength steel sheets in cars has increased progressively as an effective means to improve fuel efficiency and passenger safety [1–3]. In a steel sheet, high strength in addition to remarkable formability is desirable for conventional forming operations. Since there is a general

trend in the tradeoff between strength and other properties related to formability [4–7], steel manufacturers have invested substantial efforts into developing advanced high-strength steels (AHSSs) with improved balance among their mechanical properties [8–12]. A common approach adopted to achieve this is the design of multiphase microstructures. Different phases such as ferrite, bainite, martensite, and austenite behave differently against applied deformation, and complementary interactions among them can help mitigate the strength-formability tradeoff [4, 13–15].

To design an optimum constitution of the phases, it is essential to understand the heterogeneous deformation behavior of multiphase microstructures. Thus, various in situ and ex situ analyses of deforming microstructures have been implemented [16–20]. The application of the digital image correlation (DIC) technique led to an improvement in the effectiveness of these analyses [20–23]. With DIC, the local distribution of strain on a surface can be quantified along strain paths, and the heterogeneous pattern of deformation can be correlated with various microstructural features, such as constituent phases and grain boundaries [24]. Additionally, the combination of DIC with electron backscatter

✉ Jun-Yun Kang
firice@kims.re.kr

✉ Heung Nam Han
hnhan@snu.ac.kr

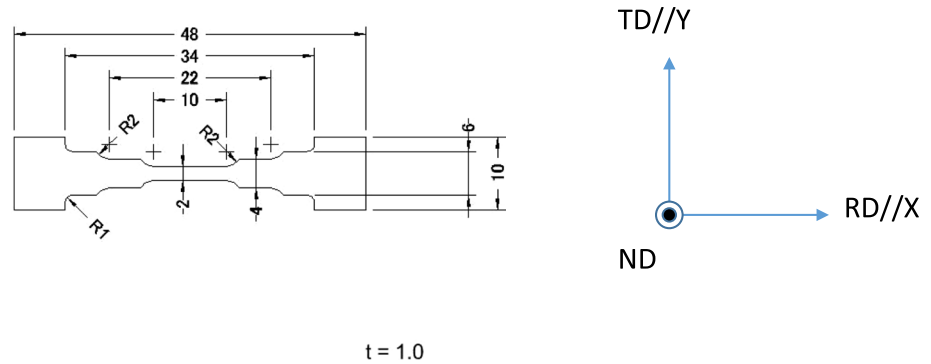
¹ Department of Materials Science and Engineering, Research Institute of Advanced Materials, Seoul National University, 08826 Seoul, Republic of Korea

² Research Institute of Advanced Manufacturing and Materials Technology, Korea Institute of Industrial Technology, 21999 Incheon, Republic of Korea

³ Korea Institute of Materials Science, 51508 Changwon, Republic of Korea

⁴ Department of Electrical and Computer Engineering, Seoul National University, 08826 Seoul, Republic of Korea

Fig. 1 **a** Deformation stage and **b** dimensions of small tensile specimen (RD: rolling direction, TD: transverse direction, ND: normal direction, X & Y: horizontal and vertical direction of micrographs)



diffraction (EBSD) analyses provided crystallographic information and revealed the microstructural features more clearly, thus strengthening the understanding of the deformation behavior [25, 26]. However, the general DIC methods reported in [27] require a random pattern on the surface to track the displacement, which makes it difficult to analyze the microstructure of a specific area covered by the pattern.

In this study, the deformation behavior of an AHSS, consisting of several phases with different mechanical characteristics, was analyzed with the aid of an in-situ deformation stage and EBSD. The local strain tensors were obtained using a DIC technique applied to the microstructural images acquired from a forescatter diodes (FSD) attached to a scanning electron microscope (SEM). The heterogeneous distribution of the strain was correlated with the microstructural features specified by EBSD mappings, with an emphasis on its correlation with the distribution of the different phases. Furthermore, the deformation of each phase was evaluated quantitatively, and the strain at the boundary of each phase was investigated to determine the interactions between the different phases.

2 Experimental Procedure

2.1 Specimen Preparation and In-Situ Tensile Test

The material investigated in this study was a TRIP-aided multiphase AHSS with yield stress, tensile stress, and elongation of 611 MPa, 1123 MPa, and 17%, respectively, with a chemical composition of Fe-0.248, C-1.88, Si-0.812, Mn-0.983, Cr-0.983 (in wt%). A 50-kg ingot was prepared by vacuum induction melting. It was then reheated to 1400 °C, held for 1 h in an atmosphere of argon, and rough rolled in a rolling mill from 30-mm- to 3.32-mm-thick plates in five passes.

The specially designed experimental setup for in-situ tensile testing using TSL solutions K.K.TS-2000. Figure 1 shows the dimensions of the tensile specimens [28]. The dog-bone-shaped specimen was extracted from the region of

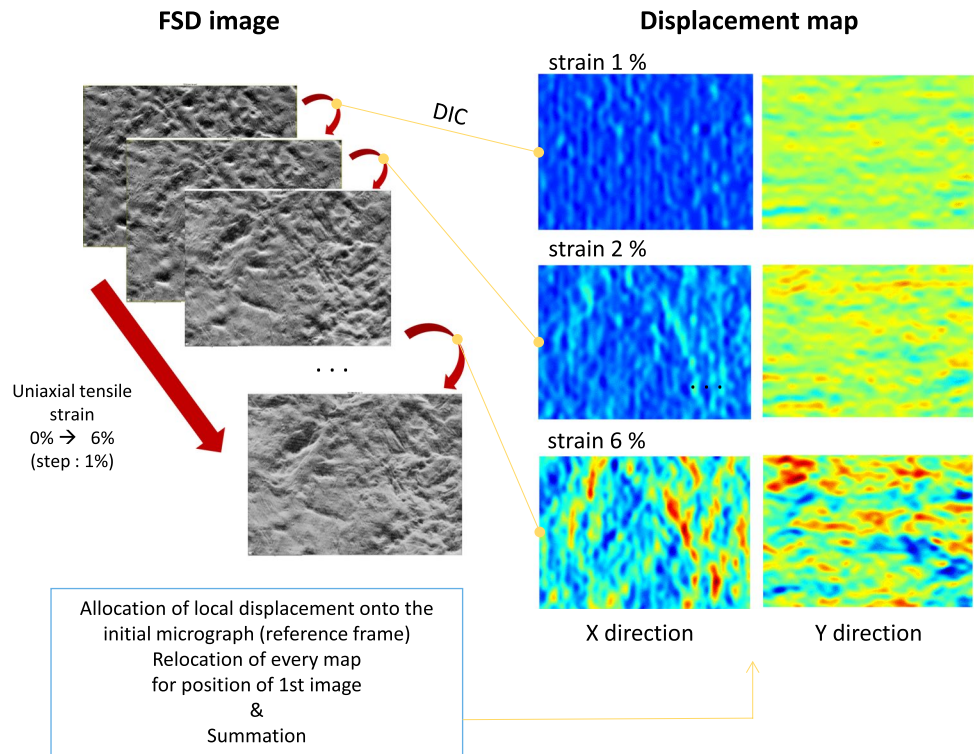
mid-thickness of the rolled plate having tensile axis parallel to the rolling direction. It was ground with silica papers and polished successively with 6- μ m and 1- μ m diamond suspensions. Finally, it was electropolished with a 10% perchloric acid 90% ethanol solution using a Struers Lectropol-5 apparatus. Electropolishing was performed at 23 °C for 15 s with a 17 V bias.

The uniaxial tensile test and in-situ EBSD experiments were performed with a crosshead speed of 6 μ m/min in a JEOL JSM-7001 F SEM equipped with a NordlysNano EBSD detector and Aztec software (Oxford Instruments). The tensile axis was along the horizontal direction in the SEM micrographs. Although a total elongation of 12% could be attained, the test was stopped at 6% due to the development of wrinkles on the surface, which interrupted clear observation by SEM. At every 1% increment in elongation, a topographic image of the surface was recorded using the FSD on the EBSD detector. The resolution of the FSD images for the observation surface were 1988 \times 1492 pixels. At every 2% increment in elongation, EBSD mapping was performed. Each mapping was performed on 497 \times 373 square grids with a step size of 0.08 μ m, thus having one-fourth the resolution of the corresponding FSD image.

2.2 Nano-indentation for Phase Classification

Constituent phases of the examined surface before straining were classified based on the EBSD map, as described in Sect. 3.1. To verify the classification, other areas of the initial state were subjected to EBSD scans followed by classification procedures. Subsequently, nano-indentation using a Hysitron TI750L nano indenter was performed on these areas to evaluate the nano hardness of the constituent phases. Manual as well as automated indentation processes were performed to assess the mechanical response of individual phases. The automated one produced a large set of data on a regular square grid of 10 \cdot 10 pixels. However, only a small part that was within the single-phase domains was usable. For more accurate data on the desired grains, the manual process was implemented with the aid of scanning probe

Fig. 2 A schematic illustration of the DIC procedure



microscopy (SPM), in which the individual phase domains revealed on the EBSD maps could be directly located and subsequently indented. All measurements were conducted in the load control made with a constant loading and unloading rate of $\pm 400 \mu\text{N s}^{-1}$ and a maximum load of $4000 \mu\text{N}$.

2.3 Estimation of Local Strain via DIC

During the in-situ tensile test, the local strain on the observation surface was estimated using a DIC technique. Conventional DIC methods depend on artificial markers printed on the surface of the specimen [27, 29–33], which limits the use of various microscopy tools such as EBSD. Therefore, a computer vision technique that can find the correspondences between varying micrographs by deformation would be helpful. In this study, the regular sparse correspondence method [34] was applied to track the displacement field on the FSD images. This method utilizes regularly spaced control points with features described by scale-invariant feature transform [35]. In the absence of artificial markers, the deformation of the specimen surface was efficiently recognized on successive FSD images.

Using this method, the displacement along the horizontal (X) and vertical (Y) directions could be mapped onto the initial micrograph (i.e., reference frame), as illustrated in Fig. 2. The displacement maps were resized to the size

of the EBSD maps (497×373 pixels) and smoothed using a Gaussian filter with a kernel size of 31×31 pixels and a standard deviation of 5 [36].

For each pixel on the displacement map, eight surrounding pixels were used for strain calculation (Fig. 3). To determine strain, a deformation gradient tensor was obtained from the displacement map as follows.

$$\mathbf{F} = \begin{bmatrix} F_{XX} & F_{XY} & F_{XZ} \\ F_{YX} & F_{YY} & F_{YZ} \\ F_{ZX} & F_{ZY} & F_{ZZ} \end{bmatrix} = \begin{bmatrix} \frac{\partial x}{\partial X} & \frac{\partial x}{\partial Y} & \frac{\partial x}{\partial Z} \\ \frac{\partial y}{\partial X} & \frac{\partial y}{\partial Y} & \frac{\partial y}{\partial Z} \\ \frac{\partial z}{\partial X} & \frac{\partial z}{\partial Y} & \frac{\partial z}{\partial Z} \end{bmatrix} \quad (1)$$

where X, Y, Z are the coordinates before deformation, and x, y, z are those after deformation. Additionally, DIC analysis was performed for an arbitrary deformation in two dimensions along the X and Y directions, as shown in Fig. 3. The following relationships hold [37].

$$F_{XX} = \frac{\overline{D'E'_X}}{DE_X} = \frac{dX_E - dX_D + 2}{2} = \frac{dX_E - dX_D}{2} + 1 \quad (2)$$

$$F_{YY} = \frac{\overline{B'G'_Y}}{BG_Y} = \frac{dY_B - dY_G + 2}{2} = \frac{dY_B - dY_G}{2} + 1 \quad (3)$$

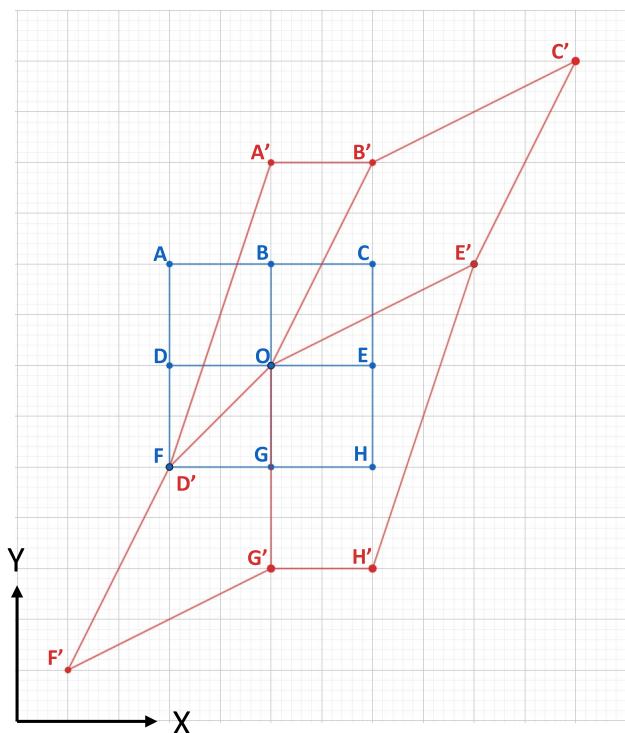


Fig. 3 Displacement of unit cell (Blue: original, Red: deformed). (Color figure online)

direction, F_{ZZ} is calculated to obtain a 3D deformation gradient tensor. Additionally, the polar decomposition with a rotation matrix and stretch tensor is given by

$$\mathbf{F} = \mathbf{R} \cdot \mathbf{U} \tag{6}$$

From this, the strain tensor considering rotation is calculated as

$$\boldsymbol{\epsilon} = \mathbf{U} - \mathbf{I} \tag{7}$$

From this strain tensor, the strains in X-, Y-, and Z-directions, i.e., ϵ_{XX} , ϵ_{YY} , and ϵ_{ZZ} , respectively, and the shear strain ϵ_{XY} can be calculated [39, 40]. In this study, the maximum shear strain (MSS), an appropriate metric for analyzing strain localization [41] was evaluated as follows.

$$MSS_{XY} = \sqrt{\left(\frac{\epsilon_{XX} - \epsilon_{YY}}{2}\right)^2 + \epsilon_{XY}^2} \tag{8}$$

$$MSS_{YZ} = \sqrt{\left(\frac{\epsilon_{YY} - \epsilon_{ZZ}}{2}\right)^2 + \epsilon_{YZ}^2} \tag{9}$$

$$MSS_{ZX} = \sqrt{\left(\frac{\epsilon_{ZZ} - \epsilon_{XX}}{2}\right)^2 + \epsilon_{ZX}^2} \tag{10}$$

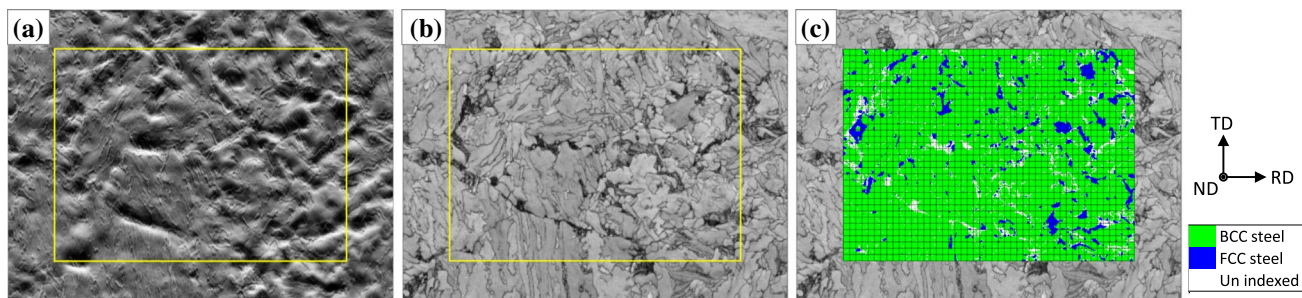


Fig. 4 Initial microstructure prior to the tensile straining: **a** FSD image, **b** band contrast (BC) map, **c** phase map (The region of interest (ROI) for the strain measurement is boxed, while in **c** a mesh is drawn with the coordinates of some pixels)

$$F_{XY} = \frac{\overline{B'G'_X}}{\overline{BG_X}} = \frac{dX_B - dX_G}{2} = \frac{dX_B - dX_G}{2} \tag{4}$$

$$F_{YX} = \frac{\overline{D'E'_Y}}{\overline{DE_Y}} = \frac{dY_E - dY_D}{2} = \frac{dY_E - dY_D}{2} \tag{5}$$

Thereafter, considering the condition that $\det(\mathbf{F}) = 1$ [38], which assumes that the unit lattice of each pixel is incompressible and that there is no shear strain in the Z

$$MSS = \max(MSS_{XY}, MSS_{YZ}, MSS_{ZX}) \tag{11}$$

3 Results

3.1 Microstructure and Phase Classification

Figure 4 shows the initial microstructure of the examined surface with the region of interest (ROI) for the local strain measurement. Figure 4a shows the surface topology revealed by FSD, while Fig. 4b shows the morphologic information

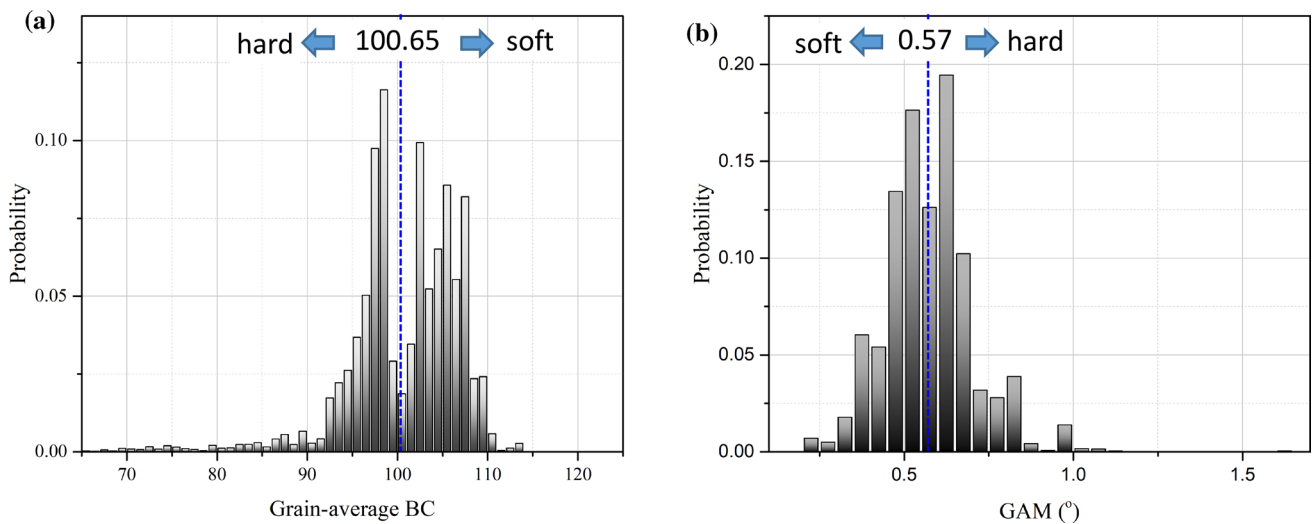


Fig. 5 Histogram of **a** grain-average band contrast (GABC) and **b** grain-average misorientation (GAM) of the region excluding austenite (γ) and martensite (α_m) with the mean values marked

revealed by the band contrast (BC) of EBSD patterns (EBSP), which is affected by defect distribution [42, 43]. Figure 4c shows the raw phase map of the ROI, which differentiates the face-centered cubic (FCC) phase from the body-centered cubic (BCC) phases. The latter includes body-centered tetragonal (BCT) phases of small tetragonality, which conventional EBSD fails to detect. In Fig. 4c, an additional mesh was drawn on the phase map with the coordinates of some pixels.

Four types of constituent phases were identified in the given microstructure. The FCC phase shown in Fig. 4c corresponds to the retained austenite (γ). The remaining regions of the BCC phase or regions having no crystallographic index were divided into the acicular ferrite phase (α_1), bainitic ferrite phase (α_2), and martensite (α_m). In this study, the procedures used by Kang et al. [44] were partly adopted to reduce the noise in the raw data and to differentiate α_m from the other phases. Phase classification was performed on clusters¹ of pixels that were bound by misorientation angles of more than 5° or different phase indices. Then, α_m was assigned to the clusters without a crystallographic index, and the small² BCC clusters which were largely³ surrounded by other α_m and γ clusters. To differentiate between α_1 and α_2 , two criteria, namely, grain-average misorientation (GAM) and grain-average BC (GABC), were adopted in a complementary manner. The former is defined by the average misorientation angles between all adjacent pixels within a

grain; thus, it can be a measure of local plasticity due to phase transformation [45]. The latter is affected not only by plasticity, but also by all other types of lattice defects.

Figure 5 shows the distribution of GABC and GAM for the remaining regions of α_1 and α_2 . It would be difficult to obtain a clear threshold for each of the two factors. If two populations of distribution are assumed, the separation between them is extremely small, as seen in Fig. 5a, while it is invisible in Fig. 5b. In this study, α_2 was differentiated from α_1 with one having a larger GAM and a lower GABC than the respective averages. Thus, α_2 would be a harder product phase than α_1 , having more lattice imperfections introduced by the transformation of parent austenite at a lower temperature. Figure 6 shows the new phase map reconstructed using the classification procedure for the ROI, described in Fig. 3. Most of the matrix was composed of α_1

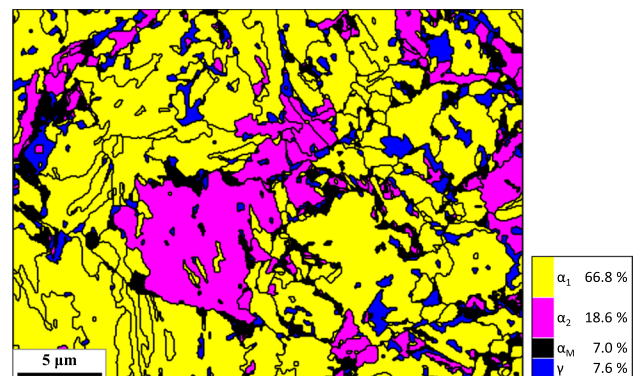


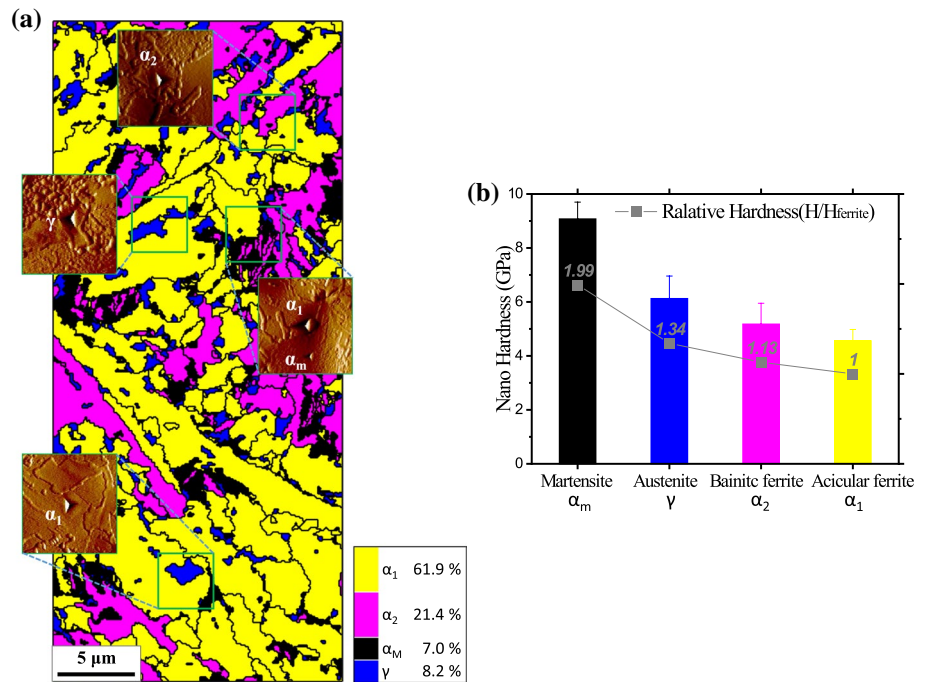
Fig. 6 Reconstructed phase map of the initial microstructure by the classification procedure (Black lines are grain or subgrain boundaries)

¹ A cluster corresponded to a grain or a sub-granular area transformed from a parent austenite grain.

² The area is smaller than the average area of all BCC clusters.

³ More than 60% of the boundary is shared with α_m and γ .

Fig. 7 Verification of phase classification via nano-indentation: **a** a few examples of the selective indentation procedure, **b** mean hardness of the phases in descending order



with a considerable fraction of α_2 , while small amounts of α_m and γ were dispersed in the matrix.

As the phase classification in this study was carried out statistically, with rather intuitive choices of criteria, the result could not be considered reliable. Thus, nanoindentation was used to verify the results. Figure 7a shows a few examples of the selective (i.e., manual) indentation on the surface area on which the EBSD mapping and the subsequent phase classification were performed previously. Figure 7b shows the average hardness of the phases calculated over all the indentations within the single-phase domains. The classification results confirmed that α_m was the hardest phase and α_1 was the softest phase.

3.2 Evolution of Microstructure and Local Strain

With the help of the displacement maps in Fig. 2, the coordinates of all the pixels within the ROI in Fig. 4b and c can be updated along the applied engineering strain (ϵ_N). Figure 8 shows the EBSD maps along ϵ_N with the updated (i.e., deformed) ROI. Thus, the effect of deformation on the microstructure can be described by the changes in the morphology and phases within the updated ROIs. The overall nature of the tensile strain, that is, the elongation along X and the contraction along Y, can be recognized by the change in the shape of the ROI. Additionally, the effect of the heterogeneous microstructure was reflected in the irregular borders of the deformed ROIs.

In the range of small ϵ_N in this specimen, the morphologic changes revealed in the BC maps are not significant enough, as seen in Figs. 4b and 8a–c, to track the ROI and

consequently check the validity of the applied DIC method qualitatively. There exist inevitable but minor errors due to the oscillation and distortion of images that originate from the instability of the SEM. Notably, the current DIC method utilizes the natural surface topography revealed by electropolishing instead of an artificial marker or stable particles such as precipitates. The former is expected to be less inert against deformation, thus rendering accurate tracking more difficult. However, the results shown in Figs. 4 and 8 verify the overall validity of the current method. In contrast to the overall morphological variations, a clear change in contrast is observed in Figs. 4b and 8a–c, which is caused by the introduction of lattice defects. This contrast change is generally more pronounced around the hard phases, that is, near α_m and γ , which indicates the localization of strain and the consequent defects around them.

The raw phase maps in Figs. 4c and 8d–f show more drastic changes compared to those in the BC maps. It is apparent that the initial γ transformed gradually into α_m , which was mostly unindexed in the raw phase maps. This transformation results in the degradation of BC around the sites of transformation and largely contributes to the aforementioned change in contrast in the BC maps. The second highest hardness of γ in Fig. 7b is attributed to the strain-induced transformation to the hardest α_m during indentation.

The estimated displacement, as shown in Fig. 2, can be transformed into MSS according to the procedure described in Sect. 2.3. The MSS at each strain step was back mapped onto the initial microstructure and thus could be placed on the EBSD map shown in Figs. 4 and 6. Figure 9 shows the resulting MSS maps at ϵ_N for the EBSD scans. It is worth

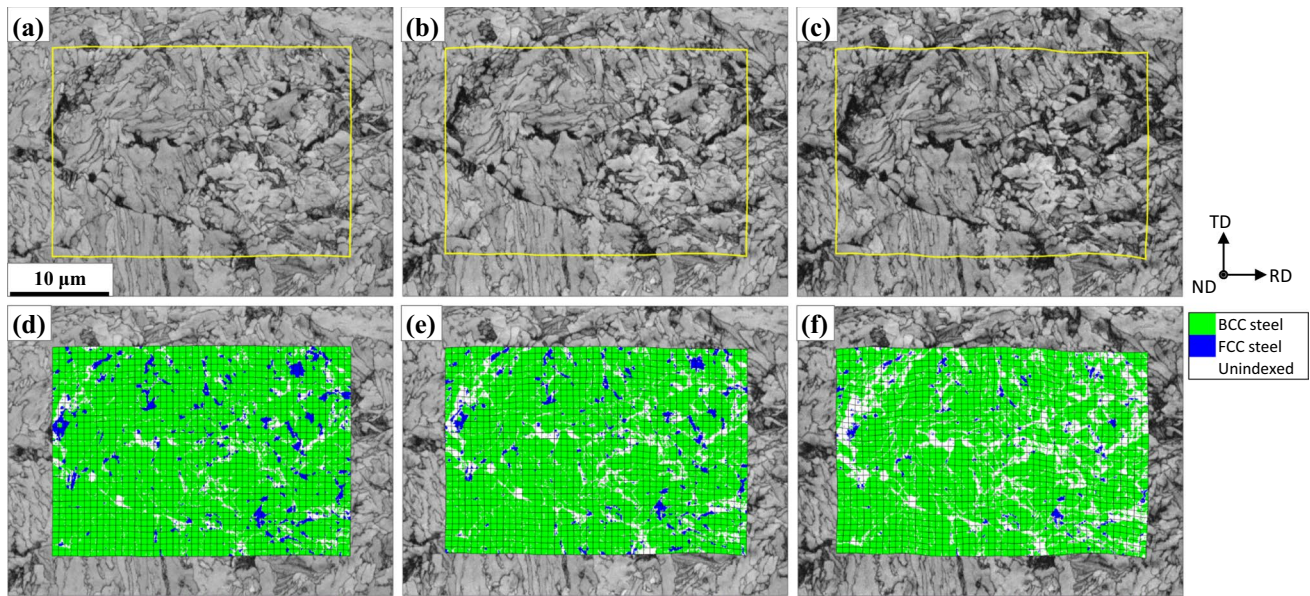


Fig. 8 Evolution of the microstructure revealed by **a–c** BC maps and **d–f** raw phase maps with applied tensile strain (ϵ_N) of **a, d** 0.02, **b, e** 0.04, **c, f** 0.06 (The deformation of ROI can be recognized by the boxes and the meshes which correspond to the initial ones in Fig. 4)

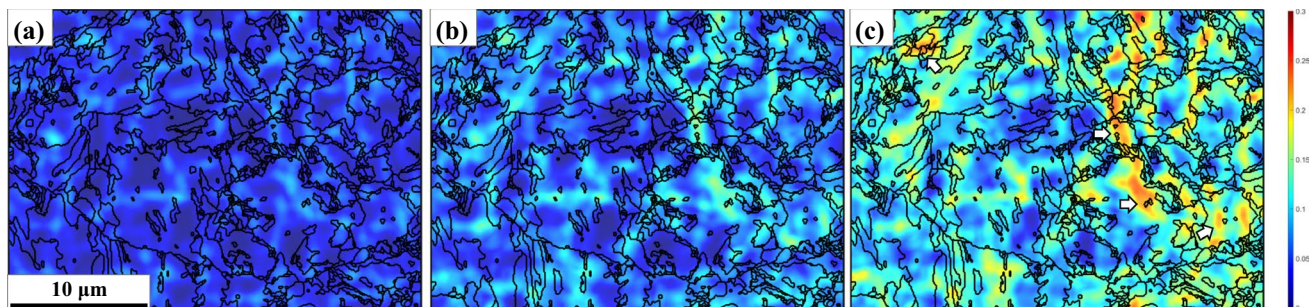


Fig. 9 MSS mapped on the initial microstructure with applied tensile strain (ϵ_N) of **a** 0.02, **b** 0.04, **c** 0.06 (black lines are grain or subgrain boundaries)

nothing that the overall levels of the estimated strain could exceed the nominal levels (i.e., ϵ_N), which is caused partly by the tendency of more strain accommodation on a specimen surface [46, 47] and also by the limited accuracy of strain measurement by DIC [48]. The heterogeneous nature of the plastic strain accommodation is shown in Fig. 9. Although the overall strain increased with ϵ_N , there was a consistent pattern of strain localization, regardless of ϵ_N . It is evident that most sites of strain localization extend across the boundaries. Some of the salient ones are marked with white arrows in Fig. 9c. In correlation with the phase map in Fig. 6, it is clearly noticeable that severe strain localization occurred around the boundaries of fine γ and α_m with α_f . Additionally, from correlation with Fig. 7b, it is understood that the strain localization was caused by the hard inclusion phase (i.e., γ and α_m) surrounded by a soft matrix (α_f). To

examine the strain level more visually, the individual phase map is shown in Fig. 10.

4 Discussion

Strain localization is inevitable when a microstructure consists of multiple phases with different mechanical properties. To maintain continuity, a soft phase should develop regions of localized strain around interfaces with hard phases. The severity of the localization increases with the difference in the mechanical properties between adjoining phases [19, 21, 49, 50]. Qualitatively, these typical features could account for the heterogeneous patterns of strain accommodation shown in Figs. 9 and 10.

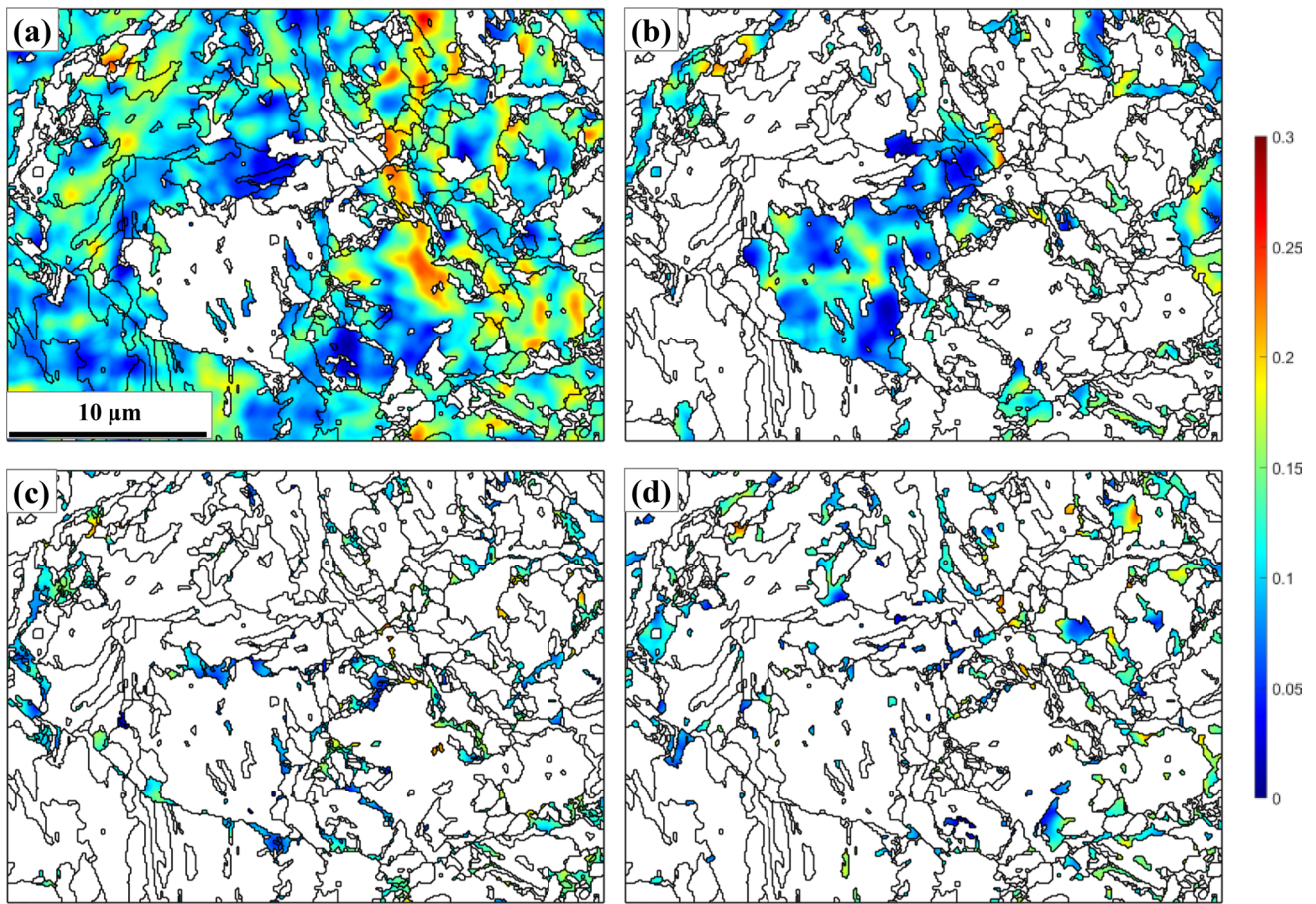


Fig. 10 MSS maps of individual phases at $\varepsilon_N=0.06$: **a** α_1 , **b** α_2 , **c** α_m , **d** γ

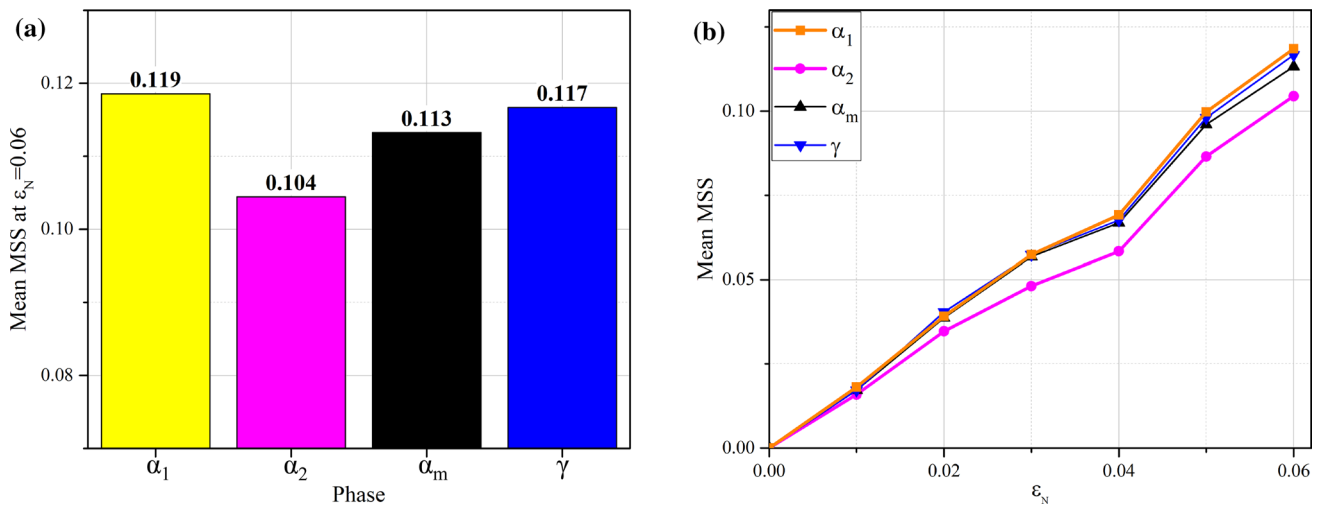


Fig. 11 Mean MSS of phases: **a** the values at $\varepsilon_N=0.06$, **b** the evolution of the values with ε_N

A quantitative analysis through the correlation of Figs. 9 and 10 with Fig. 6 was also possible. The distribution of plastic strain could be read separately on the individual

phases and thus compared quantitatively. Figure 11a shows the mean MSS per pixel of the individual phases at $\varepsilon_N=0.06$, while 11b shows their evolution and confirms the

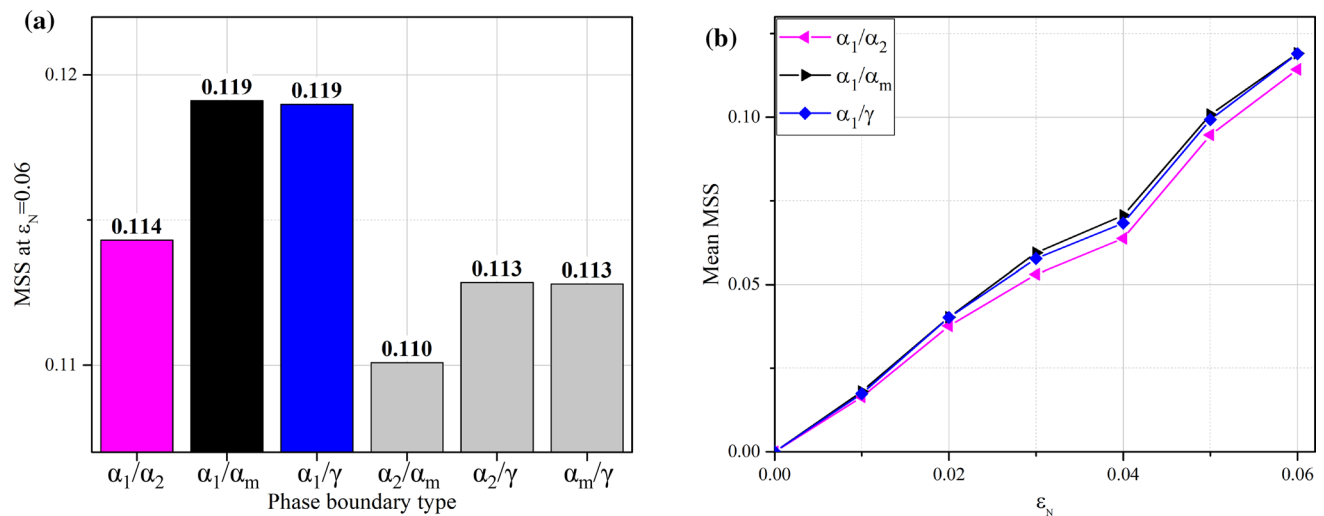


Fig. 12 Mean MSS at phase boundaries: **a** the values at $\varepsilon_N = 0.06$, **b** the evolution of the values only for those by α_1 with ε_N

consistency with ε_N . The almost linear relationship, seen in Fig. 11b, supports the overall reliability and stability of the applied DIC method in the given range of ε_N . Although the two matrix phases, α_1 and α_2 , exhibit a clear and rational strain partitioning between them, the large MSS of the other two phases, that is, α_m and γ , contradict their higher resistance to plastic straining as shown in Fig. 7. Thus, this may raise skepticism about the reliability of the applied method for strain measurement when considering a fine inclusion phase. Less than 20 and 31 pixels on average make up α_m and γ , respectively, while more than 253 and 147 pixels on average constitute α_1 and α_2 , respectively. Thus, the former group is much more prone to the issue of accuracy limit of the applied DIC method [51].

Apart from the probable inaccuracy due to small size, the large strain measured on α_m and γ has a definite physical origin; thus, it would never oppose the validity of this study. As shown in Figs. 6 and 9, the mean MSS of the pixels adjacent to the phase boundaries can be calculated separately according to the adjoining phases. Figure 12a presents the results at $\varepsilon_N = 0.06$, while Fig. 12b shows the consistency of the results with ε_N .⁴ It is clearly seen that a much larger strain was concentrated at the boundaries by the softest phase α_1 with hard α_m and γ , which clearly indicates a large incompatibility between these largely dissimilar phases. Thus, it can be considered that the large strain measured on α_m and γ (Fig. 11) is attributed to the accuracy limit due to the small size, as well as to the large strain concentration at their boundaries with α_1 . Although the former factor is a type of numerical or

experimental artifact, the latter is an intrinsic characteristic of a heterogeneous material under strain. In fact, the latter factor is expected to manifest and intensify the former. In Figs. 9 and 10, several local maxima of the MSS can be located within the α_1 regions near small inclusions of α_m and γ . It can be considered that the measurement of strain within these fine inclusions is strongly affected by interference with the local maxima.

The mechanically induced martensitic transformation (MIMT) of γ has been extensively utilized to improve the ductility of advanced steels [52–54]. As shown in Figs. 4, 6, and 8, the investigated steel in this study also contained a considerable amount of retained austenite, which transformed gradually during deformation. While MIMT is known to improve ductility through the delay of necking [52, 53], Fig. 12 indicates that it also provides sites of intense strain localization that can develop into cracks [55]. Meanwhile, as shown in Fig. 6, most γ grains were in contact with α_m such that the measured strain around them in Fig. 12 could be an overestimation due to the neighboring α_m . Although the current results cannot confirm whether the positive TRIP effect prevailed in the investigated steel, additional investigations focusing more on α_m and γ at a finer scale would expand the understanding of the progress of deformation in this type of advanced steel.

5 Conclusions

In this study, an in-situ strain analysis of a hot-rolled TRIP-aided steel with a multi-phase microstructure was performed. Using an image registration technique (the regular sparse correspondence method), an efficient DIC method to track the local evolution of strain can be applied without the

⁴ Figure 12b shows the data only for the phase boundaries by α_1 . This is only for better clarity of the figure, and the full set of data is consistent with Fig. 12a.

introduction of an artificial marker, which enables a useful correlation with EBSD. The phase classification on EBSD maps, which was verified by nano-indentation, enabled a detailed and quantitative analysis of strain partitioning between the different phases.

Although the precision was limited for the small portion of martensite (α_m) and austenite (γ), the overall correspondence among the deforming region of interest and between the local and the overall variation of strain indicated that the present DIC method was reliable and helpful in the analysis of materials with complex phases. For the two matrix phases, that is, acicular ferrite (α_1) and bainitic ferrite (α_2), it was able to capture the evidently larger strain partitioned into the former with lower hardness. Intense strain localization was apparent around the interfaces of α_1 with α_m and γ , which could be quantified by an additional analysis exclusively on phase boundaries and accounted for the erroneously large strain partitioned within the small α_m and γ . The metastable γ continued to transform into the hardest α_m , while developing a large strain along their interfaces with α_1 . Currently, for the present steel, it could be considered that γ played a role comparable to that of α_m in strain localization because of its metastability.

Acknowledgements J.-H. Kang was supported by the National Research Foundation of Korea (NRF) (2021M3H4A6A01049712). K. H. Oh was supported by Korea Evaluation Institute of Industrial Technology (KEIT) and the Ministry of Trade, Industry and Energy (MOTIE) of the Republic of Korea (No. 1415168877). J.-Y. Kang acknowledges the financial support of the Fundamental R&D Program of the Korea Institute of Materials Science (PNK6920). H. N. Han and Y. Oh were supported by the National Research Foundation of Korea (NRF) Grant Funded by the Korean Government (MSIT) (Nos. 2019M3D1A1079215, 2020R1A5A6017701, and 2021R1A2C3005096).

References

1. A. Grajcar, R. Kuziak, W. Zalecki, Arch. Civ. Mech. Eng. **12**, 334 (2012)
2. C. Lesch, N. Kwiaton, F.B. Klose, Steel Res. Int. **88**, 1700210 (2017)
3. M. Kleiner, M. Geiger, A. Klaus, CIRP Ann. Manuf. Techn. **52**, 521 (2003)
4. I.B. Timokhina, P.D. Hodgson, E.V. Pereloma, Metall. Mater. Trans. A **35**, 2331 (2004)
5. S. Toros, A. Polat, F. Ozturk, Mater. Design **41**, 298 (2012)
6. H. Khalatbari, A. Iqbal, X.F. Shi, L. Gao, G. Hussain, M. Hashemipour, Mater. Manuf. Process. **30**, 1354 (2015)
7. J.I. Yoon, J. Jung, H.H. Lee, J.Y. Kim, H.S. Kim, Met. Mater. Int. **25**, 1161 (2019)
8. H.L. Yi, L. Sun, X.C. Xiong, Mater. Sci. Technol. Lond. **34**, 1112 (2018)
9. J.P. Pedraza, R. Landa-Mejia, O. Garcia-Rincon, C.I. Garcia, Metals-Basel **9**, 545 (2019)
10. S. Kaar, D. Krizan, R. Schneider, C. Beal, C. Sommitsch, Metals-Basel **9**, 1122 (2019)
11. B.C. De Cooman, J.G. Speer, Steel Res. Int. **77**, 634 (2006)
12. N. Saeidi, M. Jafari, J.G. Kim, F. Ashrafizadeh, H.S. Kim, Met. Mater. Int. **26**, 168 (2020)
13. M.J. Santofimia, L. Zhao, R. Petrov, C. Kwakernaak, W.G. Sloof, J. Sietsma, Acta Mater. **59**, 6059 (2011)
14. F.G. Caballero, C. Garcia-Mateo, J. Chao, M.J. Santofimia, C. Capdevila, C.G. De Andres, ISIJ Int. **48**, 1256 (2008)
15. B.C. De Cooman, Curr. Opin. Solid State Mater. Sci. **8**, 285 (2004)
16. H. Ghadbeigi, C. Pinna, S. Celotto, J.R. Yates, Mater. Sci. Eng. A **527**, 5026 (2010)
17. S.O. Kruijver, L. Zhao, J. Sietsma, S.E. Offerman, N.H. Van Dijk, E.M. Lauridsen, L. Margulies, S. Grigull, H.F. Poulsen, S. Van Der Zwaag, J. Phys. IV **104**, 499 (2003)
18. W.S. Li, H.Y. Gao, H. Nakashima, S. Hata, W.H. Tian, Mater. Charact. **118**, 431 (2016)
19. C.C. Tasan, J.P.M. Hoefnagels, M. Diehl, D. Yan, F. Roters, D. Raabe, Int. J. Plasticity **63**, 198 (2014)
20. M.A. Tschopp, B.B. Bartha, W.J. Porter, P.T. Murray, S.B. Fairchild, Metall. Mater. Trans. A **40**, 2363 (2009)
21. B. Wattrisse, A. Chrysochoos, J.M. Muracciole, M. Nemoz-Gaillard, Exp. Mech. **41**, 29 (2001)
22. Y.H. Wang, J.H. Jiang, C. Wanintrudal, C. Du, D. Zhou, L.M. Smith, L.X. Yang, Exp. Tech. **34**, 54 (2010)
23. F. Grytten, H. Daiyan, M. Polanco-Loria, S. Dumoulin, Polym. Test. **28**, 653 (2009)
24. S.H. Joo, J.K. Lee, J.M. Koo, S. Lee, D.W. Suh, H.S. Kim, Scripta Mater. **68**, 245 (2013)
25. Y. Balit, E. Charkaluk, A. Constantinescu, Addit. Manuf. **31**, 100862 (2020)
26. C. Rehrl, S. Kleber, T. Antretter, R. Pippan, Mater. Charact. **62**, 793 (2011)
27. S.Q. Zhang, A. Godfrey, C.L. Zhang, W. Liu, D.J. Jensen, Mater. Charact. **164**, 2020332 (2020)
28. S.I. Wright, S. Suzuki, M.M. Nowell, JOM **68**, 2730 (2016)
29. E. Soppa, P. Doumalin, P. Binkele, T. Wiesendanger, M. Bornert, S. Schmauder, Comp. Mater. Sci. **21**, 261 (2001)
30. H.X. Wang, H.M. Xie, Y.J. Li, J.G. Zhu, Meas. Sci. Technol. **23**(3), 035402 (2012)
31. Y.Z. Zhang, T.D. Topping, E.J. Lavernia, S.R. Nutt, Metall. Mater. Trans. A **45**, 47 (2014)
32. K.N. Jonnalagadda, I. Chasiotis, S. Yagnamurthy, J. Lambros, J. Pulskamp, R. Polcawich, M. Dubey, Exp. Mech. **50**, 25 (2010)
33. S. Nagarajan, M.K. Jain, D.S. Wilkinson, R.K. Mishra, Opt. Laser Eng. **102**, 17 (2018)
34. B. Ahn, H.I. Koo, N.I. Cho, Image registration algorithm based on regular sparse correspondences and SIFT, in *Asia-Pacific Signal and Information Processing Association Annual Summit and Conference (APSIPA)*, Chiang Mai, 9-12 December 2014 (IEEE, Manhattan, 2014)
35. D.G. Lowe, Object recognition from local scale-invariant features, in *Proceedings of the Seventh IEEE International Conference on Computer Vision*, Kerkyra, 20-27 September 1999. vol. 2 (IEEE, Manhattan, 1999), p. 1150
36. B. Pan, Opt. Laser Eng. **51**, 1161 (2013)
37. P. Lava, S. Cooreman, D. Debruyne, Opt. Laser Eng. **48**, 457 (2010)
38. P.D.C.A.R. Haynes, J. Mater. Sci. **31**, 1843 (1996)
39. B. Pan, K.M. Qian, H.M. Xie, A. Asundi, Meas. Sci. Technol. **20**, 062001 (2009)
40. X.C. Pan, J. Gao, S.Z. Tao, K. Liu, J. Bai, J.W. Luo, Ultrasonics **54**, 990 (2014)
41. H. Na, S. Nambu, M. Ojima, J. Inoue, T. Koseki, Scripta Mater. **69**, 793 (2013)
42. S.I. Wright, M.M. Nowell, Microsc. Microanal. **12**, 72 (2006)

43. T. Maitland, S. Sitzman, in *Scanning Microscopy for Nanotechnology: Techniques and Applications*, ed. by W. Zhou, Z.L. Wang (Springer, New York, 2007), p.41
44. J.Y. Kang, D.H. Kim, S.I. Baik, T.H. Ahn, Y.W. Kim, H.N. Han, K.H. Oh, H.C. Lee, S.H. Han, *ISIJ Int.* **51**, 130 (2011)
45. S.I. Wright, M.M. Nowell, D.P. Field, *Microsc. Microanal.* **17**, 316 (2011)
46. G. Miyamoto, A. Shibata, T. Maki, T. Furuhashi, *Acta Mater.* **57**, 1120 (2009)
47. R. Balokhonov, V. Romanova, A. Panin, M. Kazachenok, S. Martynov, *Phys. Mesomech.* **21**, 32 (2018)
48. M. Mamivand, M.A. Zaeem, H.El Kadiri, *Acta Mater.* **87**, 45 (2015)
49. Q.H. Han, Y.L. Kang, P.D. Hodgson, N. Stanford, *Scripta Mater.* **69**, 13 (2013)
50. M.I. Latypov, S. Shin, B.C. De Cooman, H.S. Kim, *Acta Mater.* **108**, 219 (2016)
51. T.A. Berfield, J.K. Patel, R.G. Shimmin, P.V. Braun, J. Lambros, N.R. Sottos, *Exp. Mech.* **47**, 51 (2007)
52. H.N. Han, C.S. Oh, G. Kim, O. Kwon, *Mater. Sci. Eng. A* **499**, 462 (2009)
53. M. Soleimani, A. Kalhor, H. Mirzadeh, *Mater. Sci. Eng. A Struct.* **795**, 140023 (2020)
54. H.N. Han, C.G. Lee, C.S. Oh, T.H. Lee, S.J. Kim, *Acta Mater.* **52**, 5203 (2004)
55. S.H. Lee, S.H. Lee, S.H. Kang, H.N. Han, K.H. Oh, H.C. Lee, *ISIJ Int.* **48**, 1394 (2008)

Publisher's Note Springer Nature remains neutral with regard to jurisdictional claims in published maps and institutional affiliations.